Lithospheric structure and tectonic processes constrained by microearthquake activity at the central ultra-slow spreading Southwest Indian Ridge (49.2° to 50.8° E)

Zhiteng Yu[1,2], Jiabiao Li[1,2,*], Xiongwei Niu[1,*], Nicholas Rawlinson[3], Aiguo Ruan[1], Wei Wang[1], Hao Hu[1], Xiaodong Wei[1], Jie Zhang[1] and Yuyang Liang[1]

[1]Key Laboratory of Submarine Geosciences, State Oceanic Administration, Hangzhou, 310012, China.

[2]State Key Laboratory of Marine Geology, Tongji University, Shanghai, 200092, China.

[3]Department of Earth Sciences – Bullard Labs, University of Cambridge, Cambridge CB3 0EZ, UK

Corresponding authors: J. Li (jbli@sio.org.cn) and X. Niu (xwniu@sio.org.cn)

Key Points

- A thick brittle lithosphere, ~20 km thick, is revealed by the microseismicity at the ultra-slow spreading SWIR.
- The presence of an active detachment fault geometry is confirmed in the Dragon Flag hydrothermal vent field.
- A seismic gap at the centre of magmatic segment 27 is new evidence for a large magma supply.

Abstract

Beneath ultra-slow spreading ridges, the oceanic lithosphere remains poorly understood. Using recordings from a temporary array of ocean bottom seismometers, we here report a ~17-days-long microearthquake study on two segments (27 and 28) of the ultra-slow spreading Southwest Indian Ridge (49.2° to 50.8° E). A total of 214 locatable microearthquakes are recorded; seismic activity appears to be concentrated within the west median valley at segment 28 and adjacent nontransform discontinuities (NTDs). Earthquakes reach a maximum depth of ~20 km beneath the seafloor, and they mainly occur in the mantle, implying a cold and thick brittle lithosphere. The relatively uniform brittle/ductile boundary beneath segment 28 suggests that there is no focused melting in this region. The majority of earthquakes are located below the Moho interface, and a 5-km-thick aseismic zone is present beneath segment 28 and adjacent NTDs. At the Dragon Flag hydrothermal vent field along segment 28, the presence of a detachment fault has been inferred from geomorphic features and seismic tomography. Our seismicity data show that this detachment fault deeply penetrates into the mantle with a steeply dipping (~65°) interface, and it appears to rotate to a lower angle in the upper crust, with ~55° of rollover. There is a virtual seismic gap beneath magmatic segment 27, which may be connected to the presence of an axial magma chamber beneath the spreading centre as well as focused melting; in this scenario, the increased magma supply produces a broad, elevated temperature environment which suppresses earthquake generation.

Key words: Microearthquake; Southwest Indian Ridge; Detachment fault; Axial magma chamber; Lithospheric structure

1. Introduction

Along ultra-slow spreading ridges, which represent an end-member of mid-ocean ridge (MOR) systems, conductive cooling is thought to lead to a drastic reduction in mantle melt generation (Bown & White, 1994; Dick et al., 2003). The Southwest Indian Ridge (SWIR), with an average full-spreading rate of ~14 mm/yr (Patriat & Segoufin, 1988), is notable for having a variable along-axis melt supply (Cannat et al., 2008). Along the SWIR, the dominance of tectonic extension during crustal accretion with a low magma budget has been extensively documented e.g., the presence of thin crust (Cannat et al., 2006; Minshull et al., 2006) and mantle-derived peridotites on the seafloor (Dick et al., 2003; Sauter et al., 2004; Zhou & Dick, 2013; Sauter et al., 2013). Previous studies on the central and shallowest part of the SWIR crustal structure have revealed many new discoveries e.g., the first active high-temperature hydrothermal vent field on an ultra-slow spreading ridge (Tao et al., 2012); a locally corrugated oceanic core complex (Dragon Flag OCC) (Zhao et al., 2013); an extremely thick crust (~10 km) (Li et al., 2015; Niu et al., 2015) and an axial magma chamber (AMC) (Jian et al., 2017b). However, due to the lack of direct seismic evidence, understanding the lithospheric structure of ultra-slow spreading ridges is still a major challenge for MOR research.

Microearthquakes usually result from brittle processes and occur in the region above the brittle to ductile transition. Micro-seismic monitoring of mid-ocean ridges by ocean bottom seismometers (OBSs) has been widely used on MORs with a variety of spreading rates; this has proven to be a direct and efficient approach to advance our understanding of hydrothermal activity (Tolstoy et al., 2008; Bohnenstiehl et al., 2008), faulting modes (deMartin et al., 2007; Parnell-Turner et al., 2017), tectonic extension (Toomey et al., 1988; Smith et al., 2002; Tilmann et al., 2004; Läderach et al., 2011), lithosphere deformation (Schmid & Schlindwein, 2016) and magmatic

processes (Dusunur et al., 2009; Wilcock et al. 2009; Schlindwein et al., 2013). To date, only two long-term OBS experiments have been carried out along the SWIR; one at the western end (Schmid & Schlindwein, 2016) and the other at the eastern end (Schlindwein & Schmid, 2016; Schmid et al., 2017). Our study represents the first long-term study of microearthquake activity along the central SWIR.

In February 2010, a 40 station OBS network was deployed on ridge segments 27-29 (Figure 1a), as defined by Cannat et al. (1999), to determine the underlying crustal structure (Figure 1b). As well as recording air-gun sources, the OBSs were also deployed for a sufficient length of time to record a useful volume of continuous microearthquake data. In the work that follows, we present a detailed analysis of the microseismicity on the shallow central section of the SWIR between 49.2° E and 50.8° E (Figure 1a). A new three-dimensional P wave velocity model of segments 27-28, based on first arrival traveltime inversion, is also developed and used to improve the accuracy of event locations. The local microseismicity sheds new light on lithosphere structure, thermal state, detachment faulting and focused melting of the shallow central part of the SWIR.

2. Geological Setting

The SWIR represents a major boundary separating the southern Antarctic plate and the northern African plate, and extends ~7700 km (Chu & Gordon, 1999) from the eastern Bouvet triple junction to the western Rodrigues triple junction (Figure 1a). The bathymetric data show an average ocean depth of ~3200 m beneath the centre of the ridge, compared to the deeper westernmost (~4000 m) and easternmost (~4500 m) portions of the SWIR (Sauter et al., 2001; Cannat et al., 2008). Regional shallow axial depths between the Indomed (46° E) and Gallieni (52°20′ E) Transform Faults (TFs) are well correlated with negative Mantle Bouguer Anomalies (MBAs) (Georgen et al., 2001; Cannat et al., 2008) and low basalt Na_8 content (Na corrected for

fractional crystallization) (Cannat et al., 2008), indicating a thicker crust and a relatively robust melt supply (Cannat et al., 2008; Zhao et al., 2013). Nevertheless, extensive exposures of mantle peridotites in the rift mountains flanking the Gallieni FZ, which point to thin or possibly absent crust (Zhou & Dick, 2013), suggest that the shallow bathymetry on the Marion Rise is related to an isostatic response to the highly depleted mantle (Zhou & Dick, 2013).

The study region discussed here lies between the Indomed and Gallieni TFs at the centre of the SWIR where the ridge axis has an overall obliquity of 15°, and is devoid of any long-lived discontinuities (Figure 1a). A 19.5 km long nontransform discontinuity (NTD) is located west of segment 28 (Figure 1b). Segments 27 and 28 are separated by a small NTD that manifests as a deep basin (Figure 1b). Our study area includes segments 28 and 27 (49.2° to 50.8° E), which display contrasting tectonic and magmatic processes. The existence of the Dragon Flag hydrothermal vent (37° 47′ S, 49° 39′ E) was confirmed in 2007 (Tao et al., 2012) and is located at segment 28 next to a detachment fault termination (Zhao et al., 2013) which may provide a heat-circulation channel from the upper mantle (Yu et al., 2013). A low crustal magnetization zone was defined by Zhu et al. (2010) and was likely induced by hydrothermal alteration (Zhu et al., 2010; Tao et al., 2017). Along the 72 km long segment 27, the axial depth decreases to below 2 km, ~1 km shallower than the adjacent ridge sections (Figure 1b), and an extinct hydrothermal vent was discovered near the spreading centre (Tao et al., 2012). Segment 27 shows a low MBA from satellite-derived gravity anomalies (Sauter et al., 2001; 2009; Zhang et al., 2011), indicating the presence of thicker crust compared to adjacent NTDs. The refraction seismic data have also revealed anomalously thick crust of up to 10 km thick at the segment centre (Li et al., 2015; Niu et al., 2015). The presence of an axial magma chamber was inferred by the presence of a large low-velocity anomaly in the lower crust beneath the segment centre (Jian et al., 2017b),

suggesting a more strongly focused magmatic process.

3. Seismic Experiment and Data Processing

3.1. Acquisition of active and passive seismic data

In February 2010, during the cruise DY115-21 of Chinese R/V Dayang Yihao, a 3-D refraction seismic experiment involving 40 OBSs deployed on the ridge section between 49°17′ E and 50°49′ E was conducted in order to determine the underlying crustal architecture. The seismic source was a 4×24.5 L air-gun array shot at a pressure of 10.79 MPa every 80–120 s, giving an average shooting interval of 200–300 m. A total of 10,832 shots were fired during the acquisition of ~2650 km of survey lines. 38 OBSs were successfully recovered (Figure 1b). Five OBSs did not record any usable data. The active seismic data are used to obtain tomographic images of segments 27-28.

In addition to the active source dataset, the OBS array also recorded passive seismic data. The longest record was ~21 days, and the average continuous recording period for all 33 OBSs was ~17.5 days. A correction was applied to preliminary OBS locations on the seafloor by inverting the direct water-wave travel times using the method of Ao et al. (2010). The internal clocks of the OBSs were synchronized prior to deployment and following recovery, and a linear clock drift was applied to improve timing accuracy.

3.2. Earthquake detection and location with HYPOSAT

P wave and S wave arrival times from local earthquakes were picked manually in the intervals between air-gun signals on the vertical components, and their picking errors are estimated to vary between 0.05 s and 0.3 s, respectively (Figure 2). A 5-25 Hz band-pass filter was applied to all traces prior to picking (Figure 2). We detected 805 microearthquakes on 33 OBSs, each of

which was recorded by at least three stations. We first used the least-squares HYPOSAT routine (Schweitzer, 2001) to locate the 805 detected events based on a reference 1-D velocity model. Several P wave velocity models have been produced from the active-source seismic data (e.g., Zhao et al., 2013; Li et al., 2015; Niu et al., 2015; Jian et al., 2017b), and we took their average value for the shallow part (<10 km depth) of the 1-D velocity model in Figure 3. For the remainder of the model (>10 km depth), P wave velocities linearly increase to 8.04 km/s at 50 km depth (Figure 3) (Kennett, 1991). The Vp/Vs ratio was kept fixed at $\sqrt{3}$ and all event locations include an estimate of their 95% confidence interval. In total, 247 events were found to have depth errors of < 10 km and RMS travel time residuals of < 0.5 s (Figure 4); these events were selected for further processing and interpretation.

3.3. Tomography method and model evaluation

Recently Zhao et al. (2013) and Jian et al. (2017a) conducted three-dimensional (3-D) P wave tomography of segment 28 and 27, respectively. However, the two models, which are obtained using different methods, are difficult to merge to cover our study region and all available shot lines are not used in both studies. Since we wish to improve earthquake location in a region which spans the boundary between the two models, we found it necessary to produce a new 3-D tomographic model. We invert active source first arrival traveltimes using a tomography code based on the regularized least squares approach (Hobro et al., 2003) in which the conjugate gradient (CG) method is adopted to solve the inverse step (Hobro et al., 2003). The vertical component data were used for traveltime picking after band-pass filtering between 4 Hz and 20 Hz (Figure S1). In this study, we concentrate exclusively on P wave first arrivals (Figure S1) without differentiating between crustal and mantle refracted phases (Pg and Pn). The traveltime picking uncertainty varied between 50 ms to 200 ms, and generally increased with offset. For a

158 linearised solution to a non-linear inverse problem, a starting model that is reasonably close to
159 the final solution is required. If the starting model is too distant from the true structure, then the
160 inversion scheme may not converge to the desired solution. Our starting model is based on a 2-D
161 velocity profile along-strike of the ridge which was produced using 2-D traveltime tomography
162 (Niu et al., 2015; Li et al., 2015). Our initial model consisted of two layers, a water layer and a
163 crustal layer, which are separated by the seafloor interface. To accurately account for variations
164 in bathymetry, we take advantage of high-resolution multi-beam data (Figure S2, Sauter et al.,
165 2004). Velocity in the water layer was kept fixed at 1.5 km/s, and velocities in the crustal layer
166 varies between 1.8 km/s and 8.0 km/s. The velocity grid spacing for the inversion was set to 5.0
167 km and 2.5 km in the EW and NS directions, respectively, and 1.0 km in the vertical direction
168 (Figure S2), resulting in a total of 30×32×16 velocity unknowns.

169 Regularization strength (λ_m) is a scalar that controls the strength of smoothing during the
170 inversion (Hobro et al., 2003). The inversion proceeded in fourteen steps. Within each step, 5
171 iterations of forward-modelling and inversion were performed with λ_m held at a constant value.
172 λ_m was then steadily reduced for the following inversion step to increase the model roughness.
173 The percentage of full optimisation adopted by the CG algorithm determines the "size" of the
174 model update attempted at each inversion iteration, which is also steadily decreased in the
175 inversion process. We ran a number of inversions to find the appropriate value of λ_m as well as
176 the percentage of full CG solution. Figure 5 shows two cross sections of the final 3-D model.
177 Table S1 shows the inversion parameters.

178 A quick way to assess the quality of fit of a model to wide-angle seismic data is to compute the
179 Chi-square misfit function (χ^2), which is the sum (over all travel times) of the ratio of the squared
180 data misfit (observed minus model prediction) and the square of the picking error. Our preferred

velocity model has a Chi-square normalized misfit χ^2 = 1.62 (compared to 5533.0 for the starting model) and a root-mean-square (RMS) traveltime residual misfit of 73 ms (compared to 4347 ms for the starting model (Figure S3) and successfully predicts 91% (94317/103645) of the traveltimes (Figure S4). The 7.0 km/s velocity contour is chosen to correspond to the bottom of Layer 3 (i.e., the Moho interface) (Zhao et al., 2013). The number of rays through each grid cell was generally greater than 300 and often exceeded 400 (Figures S5-S7).

3.4. Relocation of hypocenters with new 3-D velocity model

In order to refine our preliminary hypocenter locations, we used the location subroutine of Tomog3D (Zhao et al., 1992), which is based on the Geiger relocation method, to relocate all 247 events in the presence of the new 3-D P wave velocity model. Both P and S wave arrival times were used to relocate the hypocenters. S wave velocities were calculated from the P wave velocity model, assuming a Vp/Vs ratio of $\sqrt{3}$. Following the relocation, we selected 214 events for the final earthquake catalogue (Figure 5) based on the following criteria: (1) all events are recorded by at least three stations; (2) the depth errors are less than 5 km; (3) the horizontal errors are less than 5 km; and (4) the RMS travel time residuals are less than 0.5 s. As a result, these events have average horizontal and vertical depth errors of 1.01 km and 1.62 km respectively, with an average RMS misfit of 0.18 s. After relocation, the focal-depth errors become < 2 km for 71% of the microearthquakes in comparison to 42% of HYPOSAT solutions (Figure S8), indicating a significant improvement of the hypocenter locations. For the same earthquakes with locations determined using the 1-D velocity model (Figure 3) and the 3-D velocity model respectively, the hypocenter location differences are very small, on average 1.0 km for latitude, 1.4 km for longitude and 1.3 km for the focal depths (Figure S9), which suggests that the differences in vertical velocity gradient (below the Moho interface) between two models

do not appear to compromise location accuracy.

3.5. Focal mechanism solutions with HASH

We determine P-phase first-motion polarities from unfiltered earthquake waveform data, and input our observations into the Hash software package (Hardebeck et al., 2002), which is not sensitive to event magnitude (Hardebeck et al., 2002), in order to calculate the best focal mechanisms of the microearthquakes (Figure S10). Using a selection criterion based on an RMS fault plane uncertainty of < 35°, average misfit < 20% and mechanism probability > 60%, we obtained well-constrained focal mechanisms for two events located beneath the NTD west of segment 28 (see Figures 6 and 8). The event closest to the Dragon Flag hydrothermal vent field has a strong component of reverse faulting (Figure 6).

4 Results

4.1 3-D velocity model

The crustal structure in the study region is well recovered (Figure 7), and the primary features are similar to those identified in previous studies (Zhao et al., 2013; Li et al., 2015; Niu et al., 2015; Jian et al., 2017a, b), which supports the reliability of our results. Although we provide a brief description of our velocity model below, the main crustal anomalies have been interpreted in detail by Zhao et al., 2013 and Jian et al., 2017a; therefore we largely focus on using the 3-D model to relocate earthquakes.

In the along axis direction, the 3-D tomographic cross sections show significant lateral variations between segments 27 and 28 (Figures 7 and S11). The NTD is characterised by the presence of a thinner crust (~5 km) and lower velocities in the shallow crust compared to the adjacent spreading segments (Y = 42 km, 47 km, 50 km and 58 km in Figure S11). Segment 28 exhibits

lower velocities (~2.8 km/s) in the shallow crust in the northern ridge flank (Y = 42 km and 47 km in Figure S11) compared to velocities (~4.0 km/s) at equivalent depth to the south (Y = 58 km in Figure S11). A low velocity (LVA) in the lower crust is also observed at the centre of segment 27 (Y = 50 km in Figure 7a and 53 km in Figure S11) as previously reported by Li et al. (2015) and Jian et al. (2017b).

In the cross axis direction, segment 28 features a strong asymmetry, and the detachment fault can be clearly identified by the high velocities (X = 35 km Figures 7c; X = 30 km and 40 km in Figure S12), similar to the results of Zhao et al. (2013). For segment 27, the LVA in the lower crust is much more clearly revealed in the along axis slices (X = 97 km in Figure 7d; X = 95 km and 100 km in Figure S12), and occupies a volume of 10 km (NS) × 6 km (EW) × 6 km (Z) (Figures 7, S11 and S12).

In map view, Figure S13 shows the detachment fault associated with the OCC at segment 28. The LVA beneath segment 27 is also clearly revealed (Figures 7b and S13).

4.2. Microearthquake locations

Both the HYPOSAT solutions and relocated results show that earthquakes are most reliably detected less than 10 km outside the seismic network (Figures 4 and 5). Microearthquake occurrence was relatively continuous as a function of time during the recording period (Figure S14). The vast majority of microearthquakes occur within the median valley along segment 28 and adjacent NTDs (Figure 5). A substantial number of events occur in the upper mantle, with 68 % lying below 10 km depth (Figure 5). The deepest hypocenter within the study area is ~23 km below sea level (bsl) at the NTD west of segment 28. Earthquakes in the final event catalogue have an average focal depth of 11.1 km bsl. Only 5% of the total number of relocated events occur beneath segment 27 (east of 50.2° E) with most of them distributed towards the

edge of the segment (Figures 4 and 5). Relative to segment 28, segment 27 can be regarded as virtually aseismic.

5. Discussion

5.1. The thick brittle lithosphere

In general, the deepest microearthquakes (with reference to the seafloor) are known to occur in the crust/shallow mantle at fast/slow-spreading ridges: e.g., 1.8 km at 9°50′ N on the fast spreading East Pacific Rise (EPR) (Bohnenstiehl et al., 2008; Tolstoy et al., 2008); 4 km at 35° N on the slow spreading Mid-Atlantic Ridge (MAR) (Barclay et al., 2001); 6 km at 14°45′ N on the MAR (Grevemeyer et al., 2013); 7-8 km at 26° N and 5° S on the MAR (Kong et al., 1992; Toomey et al., 1988; Tilmann et al., 2004; deMartin et al., 2007); and 10 km at 13°20′ N on the MAR (Parnell-Turner et al., 2017). By contrast, microseismicity at ultra-slow spreading ridges tends to feature deep hypocenters: e.g., 14 km at the Lena Trough (Läderach et al., 2011); 15 km at the Segment 8 volcano of the SWIR (Schmid et al., 2017); 20 km beneath the Knipovich Ridge (Schlindwein et al., 2013) and 31 km at the Orthogonal Super-segment of the SWIR (Schmid & Schlindwein, 2016). From our results in Figures 4 and 5, the maximum focal depth is ~20 km below the seafloor (bsf), or equivalently 16 km below the Moho discontinuity. This result provides additional confirmation that deep earthquake hypocenters are associated with ultra-slow spreading ridges, and reflects the presence of a cold and thick brittle lithosphere.

5.2 The axial lithospheric structure

A cross section along the ridge axis (Figure 8) shows that earthquakes are mainly distributed below the Moho interface and down to depths of 23 km bsl. A majority of events are located in the depth range 8-18 km bsl. As with Schlindwein and Schmid (2016), we consider the

maximum hypocenter depth as equivalent to the brittle-ductile transition (cross-section A in Figure 8), which likely coincides with the 600 °C isotherm (McKenzie et al., 2005; Bohnenstiehl & Dziak, 2008; Schmid & Schlindwein, 2016). This isotherm should be shallower in magmatically-robust sections of the ridge (Schlindwein & Schmid, 2016). Sauter et al. (2001) suggested that a larger NTD will lead to a thicker lithosphere and more focused melt supply beneath the centre of segment 28. However, there is no clear evidence of an upslope distribution of seismicity towards the segment centre in either Figure 4 or Figure 5. Instead, our results show a relatively uniform base along segment 28 and adjacent NTDs (Figures 4 and 5), which suggests that no focused melting takes place beneath this segment.

In contrast to segment 27, segment 28 appears to be more dominated by tectonic processes: e.g., a low-relief segment centre (Figure 1b); a corrugated surface caused by a long-lived detachment fault (Zhao et al., 2013); and multiple escarpments and high-angle normal faults observed along the southern flank (Liang et al., 2013). Our local seismicity implies the presence of a 20-km thick brittle lithosphere, which points to a decreased magma supply and lower temperatures. The reduction in melt is also related to the development of the detachment fault at segment 28 (Zhao et al., 2013), which is expected to form when the magma supply is at a moderate level (Tucholke et al., 2008; Olive et al., 2010). Along the spreading direction, three cross sections (Figure 9) reveal deeper hypocenters beneath the west NTD than beneath segment 28 to the east, which may be an indication of cooler lithosphere and reduced melt supply. However, given that there are only three events that are significantly deeper beneath the west NTD (Figure 8), further constraints are required to verify this interpretation.

Overall, segment 28 appears to be a relatively cold segment, with substantial mantle microearthquakes distributed within the median valley, which is characterised by a thick (~20

km) brittle lithosphere. Both the NTDs and segment centre show deep earthquake activity and the lithospheric base determined by the deepest earthquakes is relatively uniform; this reflects the presence of a low temperature environment and a lack of focused melting beneath the segment centre at present day, but melt has been focused in the past due to the along-axis crustal thickness variation beneath segment 28 (thicker) and the adjacent NTDs (thinner) (Sauter et al., 2004).

5.3. The aseismic crust

The hypocenter distribution along the axial valley reveals an obvious shallow aseismic zone above the Moho discontinuity, with a thickness of ~5 km, although a small number of scattered crustal events can be observed within the Dragon Flag hydrothermal vent field and the axial valley (Figure 8). A 15-km-thick aseismic upper lithosphere has also been found at the oblique Supersegment of the SWIR (Schmid & Schlindwein, 2016), which probably reflects substantial serpentinization (Schlindwein & Schmid, 2016). Serpentinization can reduce the strength of the lithosphere and promote strain localization (Escartín et al., 1997), and a very low degree of serpentinization (10% - 15%) can cause a dramatic change in rheological behaviour, which favors the formation of large-offset and low-angle faults (Escartín et al., 2001). Under the assumption - discussed earlier - that the brittle-ductile transition is at 600 °C, we suggest that the temperatures at the base of the aseismic zone are lower than 400 °C (cf, the base of 15-km-thick aseismic lithosphere is at temperatures of 400-500 °C, according to Schmid & Schlindwein, 2016). At these temperatures, serpentine exhibits velocity-strengthening behavior at slow sliding velocities (e.g., plate motion rates) (Reinen et al., 1991; Moore et al., 1997; Chernak & Hirth, 2010; Schwartz et al., 2013). Therefore, the aseismic zone could be linked to the presence of serpentine, since velocity-strengthening behavior inhibits earthquake nucleation (Rice & Ruina,

1983). However, depending on the other rock-types present in the crust, the effects of serpentinization on the rheology of the crust can be complex, and suppression of earthquakes is not a required outcome (Moore & Lockner, 2011).

Indeed, until now, dredged rock samples between the Indomed and Gallieni TFs have yielded abundant basalts but virtually no peridotites (Sauter et al., 2004; Zhou & Dick, 2013). Both bathymetric, gravimetric data and tomographic results argue for a thick crust here (Sauter et al., 2009; Li et al., 2015; Niu et al., 2015), indicating a high magma budget, which is not consistent with the presence of peridotites or serpentinization in the crust. Our tomography results reveal high velocity anomalies beneath the detachment fault at segment 28 (Figures 7, S11 and S12), which Zhao et al. (2013) suggested is composed primarily of gabbro. Moreover, compared to the oblique Supersegment of the SWIR (Schmid & Schlindwein, 2016), which is underlain by a thick aseismic lithosphere (~15 km), our aseismic zone is thinner (~5 km). At the TAG and 13º20' detachments on the MAR, the aseismic zones are much thinner (~3 km) (deMartin et al., 2007; Parnell-Turner et al., 2017), which may indeed be a result of a mostly gabbroic crust. The gabbro and diabase outcrops have been observed on the seafloor at the TAG (Reves-Sohn et al., 2004). Based on this range of evidence, if serpentinization or exhumed peridotite are present here, it would likely represent a small proportion of the seafloor.

5.4. Seismicity beneath the Dragon Flag hydrothermal vent field

Our results provide important new constraints on the geometry of the detachment fault in the Dragon Flag vent field. From our tomographic results, significant high velocity anomalies exist in the upper crust beneath the Dragon Flag OCC (Figures 7b, S11 and S12). However, we did not detect significant levels of microseismicity on the associated fault plane at depths < 5 km bsl (Figures 9c). From our results, microearthquake activity delineates a zone of seismicity which

steepens with depth (dip of ~65°) beneath the Moho discontinuity (cross-section C in Figure 9c), but features a low-angle exposed detachment fault surface, which is consistent with rolling-hinge models (Buck, 1988), very much like that at the TAG (deMartin et al., 2007) and that at the 13°20′ N OCC on the MAR (Parnell-Turner et al., 2017). At shallower depths, the average dip of the OCC detachment fault surface is ~8-9° based on the bathymetry, then we estimate a total fault rollover of ~55° (i.e., 65° to 9°). This amount of rollover is similar to what has been estimated at other OCCs (Garcés & Gee, 2007; deMartin et al., 2007).

Beneath the Dragon Flag hydrothermal vent field, major seismic activity occurred within the 5-km-wide axial valley, with hypocenters in the ranges 6-18 km bsl (Figure 9c). This distribution is also observed in the neighbourhood of detachment faults on the MAR: e.g., TAG vent (deMartin et al., 2007), Atlantis Massif (Collins et al., 2012), Logatchev Massif (Grevemeyer et al., 2013) and the 13°20′ N OCC on the MAR (Parnell-Turner et al., 2017). Detachment faults preferentially initiate at the ridge axis when it has reduced magma supply, which results in thicker and colder lithosphere (Buck et al., 2005; Escartín et al., 2008; Smith et al., 2012). The concentration and distribution of microseismicity beneath the axial valley reflects the presence of thick lithosphere that accommodates strain localization (Escartín et al., 1997). The deeply penetrating and high-angle faults accommodate the far-field forces that drive plate separation (Parnell-Turner et al., 2017), and provide the pathway for Dragon Flag hydrothermal convection and the generation of polymetallic sulfides deposits (Yu et al., 2013; Zhao et al., 2013).

Reverse faulting is observed at the 13°20′ N OCC on the MAR (Parnell-Turner et al., 2017), which represents the accommodation of compressive stress beneath the detachment footwall. We also detected one reverse fault at depth of near the Dragon Flag hydrothermal vent field (Figures 6 and 9c). Parnell-Turner et al. (2017) speculated that the development of reverse faults is linked

363 to the maturity of the detachment fault. The lack of reverse events at the TAG field can be
364 attributed to the young detachments, which have only been active since 0.35 Ma with 3.9 km of
365 horizontal extension (Tivey et al., 2003). At the Dragon Flag area, where the OCC has been
366 active for at least 2 Ma (Zhao et al., 2013), bathymetry clearly reveals a corrugated surface on
367 the footwall (Liang et al., 2013; Yu et al., 2013; Zhao et al., 2013). In comparison to the large
368 surface area (~ 25 km by 20 km) of detachment fault, the corrugated surface (6 km by 5 km) of
369 the Dragon Flag OCC is relatively small (Zhao et al., 2013), indicating that this detachment fault
370 is still at the developmental stage of oceanic core complex evolution (Smith et al., 2006), which
371 lies between the mature 13°20′ N OCC (Mallows & Searle, 2012; Parnell-Turner et al., 2017)
372 and young TAG detachment (deMartin et al., 2007). Based on the results of Parnell-Turner et al.
373 (2017), the well-developed corrugated dome in our study area likely produces reverse faulting in
374 the footwall, in response to flexural bending stress (Buck, 1988).

375 Based on our relocation and fault mechanism work, it appears likely that the Dragon Flag
376 detachment fault is still active and deeply penetrates the lithosphere to depths of ~20 km bsl. The
377 reverse faulting is a signature of mature, active oceanic detachments, which is triggered by
378 compressive stresses. It is worth noting that our recording time is relatively short (~17 days),
379 which means that there could be some long term variability in the distribution of earthquakes.
380 However, we do locate a significant number of events, and there is no evidence of clustering in
381 time or space, which may be an indication of aftershock activity associated with a large event.
382 We also note that we have identified only one event with a reverse mechanism, and the fault
383 orientation has an uncertainty of 27°. A longer recording duration which allows for a much larger
384 number of well constrained focal mechanism calculations would help to verify the presence of
385 active reverse faulting in this region.

5.5. Lack of seismicity in magmatic segment 27

It is generally recognized that segment 27 is very different from segment 28 (Sauter et al., 2001), in particular, it is characterised by high relief and the absence of an axial valley (Figure 1b). The highly magmatic accretion in segment 27 is represented by an LVA in the lower crust (Li et al., 2015), which is recognized as an AMC (Jian et al. 2017b). Our tomography results also clearly reveal this LVA at depths of 6-12 km (see Figures 7 and S11-S13). The lack of deep seismicity (Figures 4 and 5) appears to confirm the presence of elevated temperatures at segment 27, with increased magmatic activity associated with the AMC, which acts to limit brittle failure (Cannat et al., 2003).

The occurrence of earthquakes at the edge of the AMC was also observed at the Lucky Strike segment along the MAR (Singh et al., 2006; Dusunur et al., 2009). The Lucky Strike AMC is located at approximately 3.4 ± 0.4 km depth below the sea floor and is < 7 km in length and reaches a maximum width of 2 km (Singh et al., 2006; Combier et al., 2015). At 9º50' N on the EPR, microseismicity is concentrated above the thin AMC lenses (< 500 m wide, Kent et al., 1993) located at ~1.4 km depth, which is linked to hydrothermal circulation (Tolstoy et al., 2008). The AMC of segment 27 is located at ~4 km depth, extending to ~9.5 km bsf (Jian et al., 2017b), and therefore is ~6-km thick and ~6 km wide from our tomography results (Figures 7, and S11-S13), which is larger and deeper than those along the MAR and EPR (Kent et al., 1993; Singh et al., 2006). The relatively large-scale AMC (10 km × 6 km × 6 km) has a significant effect on the local thermal structures of segment 27, and likely results in a broad elevated temperature anomaly, which impedes the occurrence of microearthquakes.

The new data show that segment 27 in its entirety (from north to south) is seismically quiet, with only a few scattered events distributed on both sides of the spreading centre (Figures 4a and 5a).

409 In comparison to segment 28, the number of earthquakes in segment 27 is ~13, representing ~5%
410 of the total number (Figure 5), hence our conclusion that it is relatively aseismic. Both the
411 HYPOSAT solutions and Tomog3D relocations reveal an upslope distribution of earthquakes
412 towards the volcanic centre on the east side (Figure 4b and 5b), similar to the seismic gap under
413 the Logachev Seamount on the Knipovich ridge (Schlindwein et al., 2013) and under the
414 Segment 8 volcano on the SWIR (Schmid et al., 2017). This result implies a decrease in the
415 elastic thickness of the lithosphere beneath the volcanic centre, which can be viewed as evidence
416 for melt focusing over segment-scale distances (Sauter et al., 2001; Schlindwein et al., 2013;
417 Schlindwein & Schmid, 2016; Schmid et al., 2017). However, fewer events occur on on the west
418 side, and there is no obvious upslope distribution to the centre of segment 27 (Figure 5b).
419 Compared to the intense seismicity under the Logachev Seamount (Schlindwein et al., 2013), the
420 number of earthquakes in this case is quite small, which is why the evidence for a seismic gap
421 beneath the volcanic centre is unclear. On the other hand, we do locate many more earthquakes
422 beneath segment 28, and the lack of events beneath segment 27 is likely robust, and not caused
423 by the survey array design or data processing. The lack of deep seismicity beneath segment 27
424 can be associated with a broad high-temperature thermal environment connected to the local
425 AMC which is likely the product of a large focused magma supply.

426 The relatively brief period of earthquake activity presented here can only offer a snapshot of the
427 seismicity generated at the SWIR; as such, we also consider Figure S15, which shows the
428 teleseismically located earthquakes determined by the reviewed International Seismological
429 Centre (ISC) (International Seismological Centre, 2014) for the period 1960 to 2014 between the
430 Indomed and Gallieni TFs. Similar to our local seismicity, earthquakes occur frequently along
431 segment 26, exhibit a gap at segment 27 and occur frequently along segment 28 (Figure S15).

The presence of this aseismic zone, supported by both our microseismic study and teleseismically recorded earthquakes, provides new evidence for the existence of an LVA and/or an AMC that has a broad influence on the local thermal structure.

6. Conclusions

A new ~17-day microearthquake dataset, coupled with 3-D traveltime tomography from active sources, provides fresh insight into the lithospheric structures beneath the SWIR. The main findings of this work are summarized as follows.

1. Microearthquakes mainly occur in the median valley between 49.3° and 50° E. The maximum hypocenter depth is ~20 km (bsf), which confirms the presence of a thick brittle lithosphere at the ultra-slow spreading ridge as previously postulated.

2. The along axis uniform lithospheric thickness between the NTDs and segment 28 indicates that melt supply at the segment centre is not focused in the present day. Segment 28 appears to be more dominated by tectonic processes (e.g., low relief segment centre, long-lived detachment fault, OCC, and widely developed normal faults) compared to segment 27, with lower temperatures and a decreased magma supply.

3. Along the ridge axis, the majority of earthquakes occurred below the Moho interface, thus delineating a 5-km-thick aseismic crust. This aseismic zone may be due to local serpentinization. At the temperatures (inferred from the maximum hypocenter depths) in the aseismic zone, serpentine exhibits velocity-strengthening behavior at slow sliding SWIR, which suppresses earthquake nucleation; however, the potentially complex rheological properties of serpentine under different conditions means that further work is required to verify the composition of the crust.

4. The detachment fault at segment 28 is likely active, with a steep dip angle of 65°. Our results suggest that it penetrates into the mantle lithosphere well below the Moho discontinuity. At shallower depths, this detachment fault rotates in the upper crust, with a rollover of ~55°. One reverse fault is detected beneath the footwall of detachment fault, which suggests a compressive stress regime in the lithospheric mantle.

5. Both the local seismicity and teleseismically recorded earthquakes reveal an aseismic zone beneath magmatic segment 27, which supports the existence of an AMC and high magma supply. The high magma budget probably results in the shallowing of the brittle-ductile transition zone and thus in the low sub-crustal seismicity. Evidence for focused melting in the form of an upslope distribution of earthquakes towards the volcanic centre is tenuous.

Acknowledgments

We thank the crew of R/V Dayang Yihao for their efforts to complete the first Chinese active-source 3-D OBS experiment in February 2010. Thanks also to Dr. Dapeng Zhao for providing us with the Tomog3D software. We thank Drs. Chongzhi Dong, Hanchao Jian, Ling Chen, Wei Wang and Yunlong Liu for thoughtful discussions. Most of the Figures are made using GMT (Wessel & Smith, 1998). This work is supported by research grants from the National Program on Global Change and Air-Sea Interaction, SOA (No. GASI-GEOGE-01) and MOST of China (No. 2016YFC0600402), the National Natural Science Foundation of China (41506048, 41576037, 41606057) and the Postdoctoral Innovation Talents Support Program of China (2018). Data for this paper and details on the 214 relocated events are available in the supporting information (ds01). The authors thank the reviewer Daniel Sauter, an anonymous reviewer, and Associate Editor and the Editor Yehuda Ben-Zion for their constructive comments.

References

Ao, W., Zhao, M., Qiu, X., Li, J. B., Ruan, A., Li, S., & Zhang, J. (2010). The correction of shot and OBS position in the 3D seismic experiment of the SW Indian Ocean Ridge. *Chinese Journal of Geophysics, 53*(6), 1072-1081.

Barclay, A. H., Toomey, D. R., & Solomon, S. C. (2001). Microearthquake characteristics and crustal Vp/Vs structure at the Mid-Atlantic Ridge, 35° N. *Journal of Geophysical Research: Solid Earth, 106*(B2), 2017-2034.

Bohnenstiehl, D. R., Waldhauser, F., & Tolstoy, M. (2008). Frequency-magnitude distribution of microearthquakes beneath the 9°50′ N region of the East Pacific Rise, October 2003 through April 2004. *Geochemistry, Geophysics, Geosystems, 9*(10).

Bown, J. W., & White, R. S. (1994). Variation with spreading rate of oceanic crustal thickness and geochemistry. *Earth and Planetary Science Letters*, *121*(3-4), 435-449.

Buck, W. R. (1988). Flexural rotation of normal faults. *Tectonics, 7*(5), 959-973.

Buck, W. R., Lavier, L. L., & Poliakov, A. N. (2005). Modes of faulting at mid-ocean ridges. *Nature, 434*(7034), 719.

Cannat, M., Rommevaux-Jestin, C., Sauter, D., Deplus, C., & Mendel, V. (1999). Formation of the axial relief at the very slow spreading Southwest Indian Ridge (49° to 69° E). *Journal of Geophysical Research: Solid Earth, 104*(B10), 22825-22843.

Cannat, M., Rommevaux-Jestin, C., & Fujimoto, H. (2003). Melt supply variations to a magma-poor ultra-slow spreading ridge (Southwest Indian Ridge 61° to 69° E). *Geochemistry, Geophysics, Geosystems, 4*(8).

Cannat, M., Sauter, D., Mendel, V., Ruellan, E., Okino, K., Escartín, J., Combier, V., & Baala, M. (2006). Modes of seafloor generation at a melt-poor ultraslow-spreading ridge. *Geology, 34*(7), 605-608.

500 Cannat, M., Sauter, D., Bezos, A., Meyzen, C., Humler, E., & Rigoleur, L. M. (2008). Spreading
501 rate, spreading obliquity, and melt supply at the ultraslow spreading Southwest Indian
502 Ridge. *Geochemistry, Geophysics, Geosystems, 9*(4).
503 Chernak, L. J., & Hirth, G. (2010). Deformation of antigorite serpentinite at high temperature
504 and pressure. *Earth and Planetary Science Letters, 296*(1), 23-33.
505 Chu, D., & Gordon, R. G. (1999). Evidence for motion between Nubia and Somalia along the
506 Southwest Indian Ridge. *Nature, 398*(6722), 64-67.
507 Collins, J. A., Smith, D. K., & McGuire, J. J. (2012). Seismicity of the Atlantis Massif
508 detachment fault, 30° N at the Mid-Atlantic Ridge. *Geochemistry, Geophysics,*
509 *Geosystems, 13*(10).
510 Combier, V., Seher, T., Singh, S. C., Crawford, W. C., Cannat, M., Escartín, J., & Dusunur, D.
511 (2015). Three-dimensional geometry of axial magma chamber roof and faults at Lucky
512 Strike volcano on the Mid - Atlantic Ridge. *Journal of Geophysical Research: Solid*
513 *Earth, 120*(8), 5379-5400.
514 deMartin, B. J., Sohn, R. A., Canales, J. P., & Humphris, S. E. (2007). Kinematics and geometry
515 of active detachment faulting beneath the Trans-Atlantic Geotraverse (TAG)
516 hydrothermal field on the Mid-Atlantic Ridge. *Geology, 35*(8), 711-714.
517 Dick, H. J., Lin, J., & Schouten, H. (2003). An ultraslow-spreading class of ocean ridge. *Nature,*
518 *426*(6965), 405.
519 Dusunur, D., Escartín, J., Combier, V., Seher, T., Crawford, W., Cannat, M., Sing, C., Matias, L.
520 M., & Miranda, J. (2009). Seismological constraints on the thermal structure along the
521 Lucky Strike segment (Mid-Atlantic Ridge) and interaction of tectonic and magmatic
522 processes around the magma chamber. *Marine Geophysical Researches, 30*(2), 105-120.

523 Escartín, J., Hirth, G., & Evans, B. (1997). Nondilatant brittle deformation of serpentinites:
524 Implications for Mohr-Coulomb theory and the strength of faults. *Journal of Geophysical*
525 *Research: Solid Earth, 102*(B2), 2897-2913.
526 Escartín, J., Hirth, G., & Evans, B. (2001). Strength of slightly serpentinized peridotites:
527 implications for the tectonics of oceanic lithosphere. *Geology, 29*(29), 1023-1026.
528 Escartín, J., Smith, D. K., Cann, J., Schouten, H., Langmuir, C. H., & Escrig, S. (2008). Central
529 role of detachment faults in accretion of slow-spreading oceanic lithosphere. *Nature,*
530 *455*(7214), 790.
531 Garcés, M., & Gee, J. S. (2007). Paleomagnetic evidence of large footwall rotations associated
532 with low-angle faults at the Mid-Atlantic Ridge. *Geology, 35*(3), 279-282.
533 Georgen, J. E., Lin, J., & Dick, H. J. (2001). Evidence from gravity anomalies for interactions of
534 the Marion and Bouvet hotspots with the Southwest Indian Ridge: Effects of transform
535 offsets. *Earth and Planetary Science Letters, 187*(3), 283-300.
536 Grevemeyer, I., Reston, T. J., & Moeller, S. (2013). Microseismicity of the Mid-Atlantic Ridge at
537 7° S–8° 15′ S and at the Logatchev Massif oceanic core complex at 14° 40′ N–14° 50′ N.
538 *Geochemistry, Geophysics, Geosystems, 14*(9), 3532-3554.
539 Hardebeck, J. L., & Shearer, P. M. (2002). A new method for determining first-motion focal
540 mechanisms. *Bulletin of the Seismological Society of America, 92*(6), 2264-2276.
541 Hobro, J., Singh, S., & Minshull, T. (2003). Three-dimensional tomographic inversion of
542 combined reflection and refraction seismic traveltime data. *Geophysical Journal*
543 *International*, *152*, 79-93.
544 International Seismological Centre. (2014). Bull. Internatl. Seismol. Cent., 36(1), Thatcham,
545 United Kingdom.

546 Jian, H., Chen, Y. J., Singh, S. C., Li, J., Zhao, M., Ruan, A., & Qiu, X. (2017a). Seismic
547 structure and magmatic construction of crust at the ultraslow-spreading Southwest Indian
548 Ridge at 50°28'E. *Journal of Geophysical Research: Solid Earth*, *122*(1), 18-42.
549 Jian, H., Singh, S. C., Chen, Y. J., & Li, J. (2017b). Evidence of an axial magma chamber
550 beneath the ultraslow-spreading Southwest Indian Ridge. *Geology, 45*(2), 143-146.
551 Kennett, B. L. N. (1992). Locating oceanic earthquakes—the influence of regional models and
552 location criteria. *Geophysical Journal International, 108*(3), 848-854.
553 Kent, G. M., Harding, A. J., & Orcutt, J. A. (1993). Distribution of magma beneath the East
554 Pacific Rise between the Clipperton transform and the 9 17′ N Deval from forward
555 modeling of common depth point data. *Journal of Geophysical Research: Solid Earth,*
556 *98*(B8), 13945-13969.
557 Kong, L. S., Solomon, S. C., & Purdy, G. M. (1992). Microearthquake characteristics of a mid-
558 ocean ridge along-axis high. *Journal of Geophysical Research: Solid Earth, 97*(B2),
559 1659-1685.
560 Läderach, C., Schlindwein, V., Schenke, H.-W., & Jokat, W. (2011). Seismicity and active
561 tectonic processes in the ultra-slow spreading Lena Trough, Arctic Ocean. *Geophysical*
562 *Journal International, 184*(3), 1354-1370.
563 Li, J., Jian, H., Chen, Y. J., Singh, S. C., Ruan, A., Qiu, X., Zhao, M., Wang, X., Niu, X., Ni, J.,
564 & Zhang, J. (2015). Seismic observation of an extremely magmatic accretion at the
565 ultraslow spreading Southwest Indian Ridge. *Geophysical Research Letters, 42*(8), 2656-
566 2663.
567 Liang, Y., Li, J., Li, S., Ruan, A., Ni, J., Yu, Z., & Zhu, L. (2013). The morphotectonics and its
568 evolutionary dynamics of the central Southwest Indian Ridge (49° to 51° E). *Acta*

Oceanologica Sinica, 32(12), 87-95.

Mallows, C., & Searle, R. C. (2012). A geophysical study of oceanic core complexes and surrounding terrain, Mid-Atlantic Ridge 13° N–14° N. *Geochemistry, Geophysics, Geosystems, 13*(6).

McKenzie, D., Jackson, J., & Priestley, K. (2005). Thermal structure of oceanic and continental lithosphere. *Earth and Planetary Science Letters, 233*(3-4), 337-349.

Minshull, T., Muller, M., & White, R. (2006). Crustal structure of the Southwest Indian Ridge at 66 E: Seismic constraints. *Geophysical Journal International, 166*(1), 135-147.

Moore, D. E., Lockner, D. A., Ma, S., Summers, R., & Byerlee, J. D. (1997). Strengths of serpentinite gouges at elevated temperatures. *Journal of Geophysical Research: Solid Earth, 102*(B7), 14787-14801.

Moore, D. E., & Lockner, D. A. (2011). Frictional strengths of talc-serpentine and talc-quartz mixtures. *Journal of Geophysical Research Solid Earth, 116*(B1), 673-690.

Niu, X., Ruan, A., Li, J., Minshull, T., Sauter, D., Wu, Z., Qiu, X., Zhao, M., Chen, Y. J., & Singh, S. (2015). Along-axis variation in crustal thickness at the ultraslow spreading Southwest Indian Ridge (50° E) from a wide-angle seismic experiment. *Geochemistry, Geophysics, Geosystems, 16*(2), 468-485.

Olive, J.-A., Behn, M. D., & Tucholke, B. E. (2010). The structure of oceanic core complexes controlled by the depth distribution of magma emplacement. *Nature Geoscience, 3*(7), 491.

Parnell-Turner, R., Sohn, R. A., Peirce, C., Reston, T. J., MacLeod, C. J., Searle, R. C., & Simão, N. M. (2017). Oceanic detachment faults generate compression in extension. *Geology, 45*(10), 923-926.

592 Patriat, P., & Segoufin, J. (1988). Reconstruction of the central Indian Ocean. *Tectonophysics,*
593 *155*(1-4), 211-234.
594 Reinen, L. A., Weeks, J. D., & Tullis, T. E. (1991). The frictional behavior of serpentinite:
595 implications for aseismic creep on shallow crustal faults. *Geophysical Research Letters,*
596 *18*(10), 1921–1924.
597 Reves-Sohn, R., Humphris, S., & Canales, J. P. (2004). Cruise report: Seismicity and fluid flow
598 of the TAG Hydrothermal Mound-4: Woods Hole, Massachusetts, Woods Hole
599 Oceanographic Institution,
600 ftp://obs.whoi.edu/pub/ras/STAG/STAG_Leg4_Cruise_Report. pdf (March 2007).
601 Rice, J. R., & Ruina, A. L. (1983). Stability of steady frictional slipping. *Journal of Applied*
602 *Mechanics, 50*(2), 343-349.
603 Sauter, D., Patriat, P., Rommevaux-Jestin, C., Cannat, M., Briais, A., & Gallieni Shipboard
604 Scientific Party. (2001). The Southwest Indian Ridge between 49 15′ E and 57 E:
605 Focused accretion and magma redistribution. *Earth and Planetary Science Letters,*
606 *192*(3), 303-317.
607 Sauter, D., Carton, H., Mendel, V., Munschy, M., Rommevaux-Jestin, C., Schott, J. J., &
608 Whitechurch, H. (2004). Ridge segmentation and the magnetic structure of the Southwest
609 Indian Ridge (at 50°30′ E, 55°30′ E and 66°20′ E): Implications for magmatic processes
610 at ultraslow-spreading centers. *Geochemistry, Geophysics, Geosystems, 5*(5).
611 Sauter, D., Cannat, M., Meyzen, C., Bezos, A., Patriat, P., Humler, E., & Debayle, E. (2009).
612 Propagation of a melting anomaly along the ultraslow Southwest Indian Ridge between
613 46° E and 52°20′ E: interaction with the Crozet hotspot? *Geophysical Journal*
614 *International, 179*(2), 687-699.

615 Sauter, D., & Cannat, M. (2010). The ultraslow spreading Southwest Indian ridge. *Diversity of*
616 *Hydrothermal Systems on Slow Spreading Ocean Ridges*, 153-173.
617 Sauter, D., Cannat, M., Rouméjon, S., Andreani, M., Birot, D., Bronner, A., Brunelli, D., Carlut,
618 J., Delacour, A., Guyader, V., MacLeod, C. J., Manatschal, G., Mendel, V., Ménez, B.,
619 Pasini, V., Ruellan, E., & Guyader, V. (2013). Continuous exhumation of mantle-derived
620 rocks at the Southwest Indian Ridge for 11 million years. *Nature Geoscience, 6*(4), 314.
621 Schlindwein, V., Demuth, A., Geissler, W. H., & Jokat, W. (2013). Seismic gap beneath
622 Logachev Seamount: Indicator for melt focusing at an ultraslow mid-ocean ridge?
623 *Geophysical Research Letters, 40*(9), 1703-1707.
624 Schlindwein, V., & Schmid, F. (2016). Mid-ocean-ridge seismicity reveals extreme types of
625 ocean lithosphere. *Nature, 535*(7611), 276-279.
626 Schmid, F., & Schlindwein, V. (2016). Microearthquake activity, lithospheric structure, and
627 deformation modes at an amagmatic ultraslow spreading Southwest Indian Ridge
628 segment. *Geochemistry, Geophysics, Geosystems, 17*(7), 2905-2921.
629 Schmid, F., Schlindwein, V., Koulakov, I., Plötz, A., & Scholz, J.-R. (2017). Magma plumbing
630 system and seismicity of an active mid-ocean ridge volcano. *Scientific Reports, 7*.
631 Schweitzer, J. (2001). HYPOSAT—An enhanced routine to locate seismic events. *Monitoring*
632 *the Comprehensive Nuclear-Test-Ban Treaty: Sourse Location* (pp. 277-289): Springer.
633 Schwartz, S., Guillot, S., Reynard, B., Lafay, R., Debret, B., Nicollet, C., Lanari, P., & Auzende,
634 A. L. (2013). Pressure-temperature estimates of the lizardite/antigorite transition in high
635 pressure serpentinites. *Lithos, 178*(9), 197-210.
636 Singh, S. C., Crawford, W. C., Carton, H., Seher, T., Combier, V., Cannat, M., Canales J. P.,
637 Düsünür, D., Escartín, J., & Miranda, J. M. (2006). Discovery of a magma chamber and

faults beneath a Mid-Atlantic Ridge hydrothermal field. *Nature, 442*(7106), 1029.

Smith, D. K., Cann, J. R., & Escartín, J. (2006). Widespread active detachment faulting and core complex formation near 13 N on the Mid-Atlantic Ridge. *Nature, 442*(7101), 440.

Smith, D. K., Escartín, J., Schouten, H., & Cann, J. R. (2012). Active long-lived faults emerging along slow-spreading mid-ocean ridges. *Oceanography, 25*(1), 94-99.

Smith, D. K., Tolstoy, M., Fox, C. G., Bohnenstiehl, D. W. R., Matsumoto, H., & Fowler, M. J. (2002). Hydroacoustic monitoring of seismicity at the slow-spreading Mid-Atlantic Ridge. *Geophysical Research Letters, 29*(11), 13-11–13-14.

Tao, C., Lin, J., Guo, S., Chen, Y. J., Wu, G., Han, X., German, C. R., Yoerger, D. R., Zhou, N., Su, X., Zhu, J., Li, H., & the DY115-19 (Legs 1–2) and DY115-20 (Legs 4–7) Science Parties. (2012). First active hydrothermal vents on an ultraslow-spreading center: Southwest Indian Ridge. *Geology, 40*(1), 47-50.

Tao, C., Wu, T., Liu, C., Li, H., & Zhang, J. (2017). Fault inference and boundary recognition based on near-bottom magnetic data in the Longqi hydrothermal field. *Marine Geophysical Research, 38*(1-2), 17-25.

Tilmann, F., Flueh, E., Planert, L., Reston, T., & Weinrebe, W. (2004). Microearthquake seismicity of the Mid-Atlantic Ridge at 5° S: A view of tectonic extension. *Journal of Geophysical Research: Solid Earth, 109*(B6).

Tivey, M. A., Schouten, H., & Kleinrock, M. C. (2003). A near-bottom magnetic survey of the Mid-Atlantic Ridge axis at 26° N: Implications for the tectonic evolution of the TAG segment. *Journal of Geophysical Research: Solid Earth, 108*(B5).

Tolstoy, M., Waldhauser, F., Bohnenstiehl, D., Weekly, R., & Kim, W. (2008). Seismic identification of along-axis hydrothermal flow on the East Pacific Rise. *Nature,*

451(7175), 181.

Toomey, D. R., Solomon, S. C., & Purdy, G. (1988). Microearthquakes beneath Median Valley of Mid-Atlantic Ridge near 23° N: Tomography and tectonics. *Journal of Geophysical Research: Solid Earth, 93*(B8), 9093-9112.

Tucholke, B. E., Behn, M. D., Buck, W. R., & Lin, J. (2008). Role of melt supply in oceanic detachment faulting and formation of megamullions. *Geology, 36*(6), 455-458.

Wessel, P., & Smith, W. H. (1998). New, improved version of Generic Mapping Tools released. Eos, *Transactions American Geophysical Union, 79*(47), 579-579.

Wilcock, W. S., Hooft, E. E., Toomey, D. R., McGill, P. R., Barclay, A. H., Stakes, D. S., & Ramirez, T. M. (2009). The role of magma injection in localizing black-smoker activity. *Nature Geoscience, 2*(7), 509.

Yu, Z., Li, J., Liang, Y., Han, X., Zhang, J., & Zhu, L. (2013). Distribution of large-scale detachment faults on mid-ocean ridges in relation to spreading rates. *Acta Oceanologica Sinica, 32*(12), 109-117.

Zhang, T., Lin, J., & Gao, J. (2011). Interactions between hotspots and the Southwest Indian Ridge during the last 90 Ma: implications on the formation of oceanic plateaus and intra-plate seamounts. *Science China Earth Sciences, 54*(8), 1177-1188.

Zhao, D., Hasegawa, A., & Horiuchi, S. (1992). Tomographic imaging of P and S wave velocity structure beneath northeastern Japan. *Journal of Geophysical Research: Solid Earth, 97*(B13), 19909-19928.

Zhao, M., Qiu, X., Li, J., Sauter, D., Ruan, A., Chen, J., Cannat, M., Sing, S., Zhang, J., Wu, Z., & Niu, X. (2013). Three-dimensional seismic structure of the Dragon Flag oceanic core complex at the ultraslow spreading Southwest Indian Ridge (49° 39′ E). *Geochemistry,*

Geophysics, Geosystems, 14(10), 4544-4563.

Zhou, H., & Dick, H. J. (2013). Thin crust as evidence for depleted mantle supporting the Marion Rise. *Nature, 494*(7436), 195.

Zhu, J., Lin, J., Chen, Y. J., Tao, C., German, C. R., Yoerger, D. R., & Tivey, M. A. (2010). A reduced crustal magnetization zone near the first observed active hydrothermal vent field on the Southwest Indian Ridge. *Geophysical Research Letters, 37*(18).

Figure Captions

Figure 1. Seismic survey area. (a) Bathymetric map of the central Southwest Indian Ridge (red curve) and fracture zones (white dashed lines) derived from ETOPO1V1. Red square denotes the present study area shown in (b). (b) Bathymetric map of the study region. The bathymetric map is extracted from the data provided in Sauter et al. (2001). The red star denotes the active Dragon Flag hydrothermal vent, and the blue star denotes an extinct hydrothermal vent (Tao et al., 2012). The white solid and dashed lines represent the spreading segments and the nontransform discontinuities (NTDs) respectively (Cannat et al., 1999; Sauter et al., 2001). The black triangles indicate the OBS stations used in this study, and the white triangles indicate the remaining OBS stations (lost or with unrecoverable data). The red lines denote the locations of the cross sections shown in Figure 7. The spreading direction is shown by white arrows, with the half spreading rate superimposed.

Figure 2. Waveforms from a typical event (which occurred on 18 February 2010) located near OBS 21 at 10.9 km below sea level. Data have been band-passed filtered between 5 Hz and 25 Hz. Blue and red markers denote P and S-phase arrival picks respectively. Station names with corresponding epicentral distances beneath are shown on the left.

707 **Figure 3.** 1-D P wave velocity model (black line) used in this study. The grey region defines the
708 range of 1-D velocity profiles extracted from a number of active wide-angle seismic profiles
709 (Zhao et al., 2013; Li et al., 2015; Niu et al., 2015; Jian et al., 2017b).

710 **Figure 4.** Distribution of earthquakes recorded by the OBSs and located using the HYPOSAT
711 code in the presence of a 1-D velocity model (see Figure 3). (a) Distribution of the 247
712 microearthquakes located in the study region. (b) East-west and (c) north-south vertical cross-
713 sections illustrating the earthquakes shown in Figure 4a. The gray dots denote the focal depths
714 below sea level (bsl) which are quantified by the scale on the right. The remaining labeling is
715 identical to that used in Figure 1.

716 **Figure 5.** Distribution of relocated earthquakes obtained using the 3-D P wave velocity model.
717 (a) Distribution of the 214 microearthquakes in the final catalogue. (b) East-west and (c) north-
718 south vertical sections showing the earthquakes displayed in Figure 5a. The red lines indicate
719 vertical section (A) in Figure 8. The remaining labeling is identical to that used in Figure 1.

720 **Figure 6**. (a) Best fitting focal mechanism solutions (red dots) for relocated events with clear P-
721 phase onset polarities at all stations. The strike, dip and rake are shown on the top of each
722 beachball, with the associated fault plane uncertainty and mechanism probability on the right.
723 The black and white shadings denote compressional and dilatational first motions, respectively.
724 (b) East-west vertical section showing the focal mechanism hypocenters (red dots) and remaining
725 relocated events (gray). The remaining labeling is identical to that used in Figure 1.

726 **Figure 7.** (a) Cross section parallel to the ridge axis from the final 3-D velocity model (locations
727 shown in Figures 1 and S2). (b) Map view of the velocity tomography; the layer depth is shown
728 in the upper-left. (c, d) Cross sections transverse to the ridge axis. Velocity contours are shown
729 every 0.4 km/s. The red star denotes the Dragon Flag hydrothermal vent. The solid and dashed

730 purple lines on the top of each figures denote the location of spreading segment centre and NTDs
731 respectively. The color scale used is shown on the right. “V.E.” is vertical exaggeration. “LVA” is
732 low velocity anomaly. “OCC” is oceanic core complex.

733 **Figure 8.** Vertical cross-section A, with the hypocenters of microearthquakes superimposed (see
734 Figure 6a for geographic location). The colored dots show all earthquakes located within 20 km
735 from the cross-section. Focal depth errors are shown using black vertical bars. The black lines
736 denote the velocity contours, and the bold lines indicate seafloor and Moho interfaces. The solid
737 and dashed purple lines represent the spreading segment centre and the NTDs. The black dots
738 denote two well-determined focal mechanism solutions shown in Figure 6.

739 **Figure 9.** Three cross sections (B, C and D) along segment 28 and adjacent NTD, with
740 geographic locations shown in (a). The solid and dashed lines (a) denote the spreading centre and
741 NTD respectively. The colored dots show all earthquakes located within 8 km of their respective
742 cross-section. The red curves denote the inferred detachment surfaces. The remaining labeling is
743 identical to that used in Figure 8.

Figure 1.

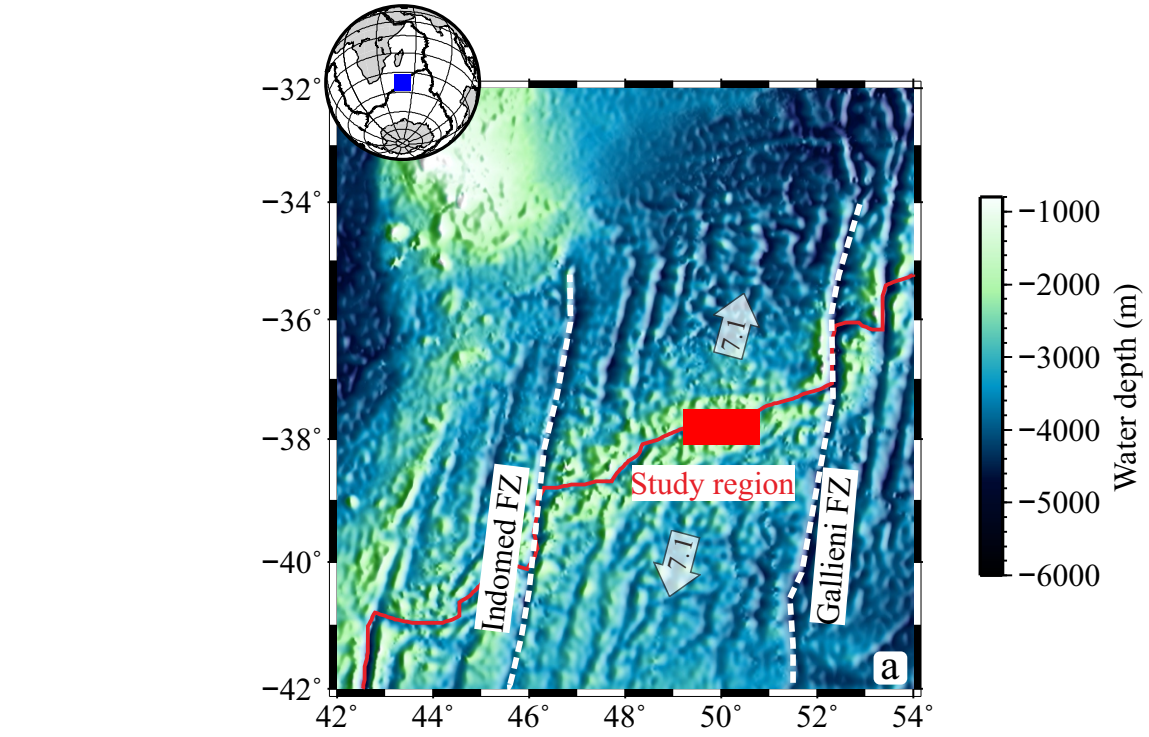
−32°
−34°
−36°
−38°
−40°
−42°
42°
44°
46°
48°
50°
52°
54°
Indomed FZ
Gallieni FZ
Study region
7.1
7.1
a
−1000
−2000
−3000
−4000
−5000
−6000
Water depth (m)

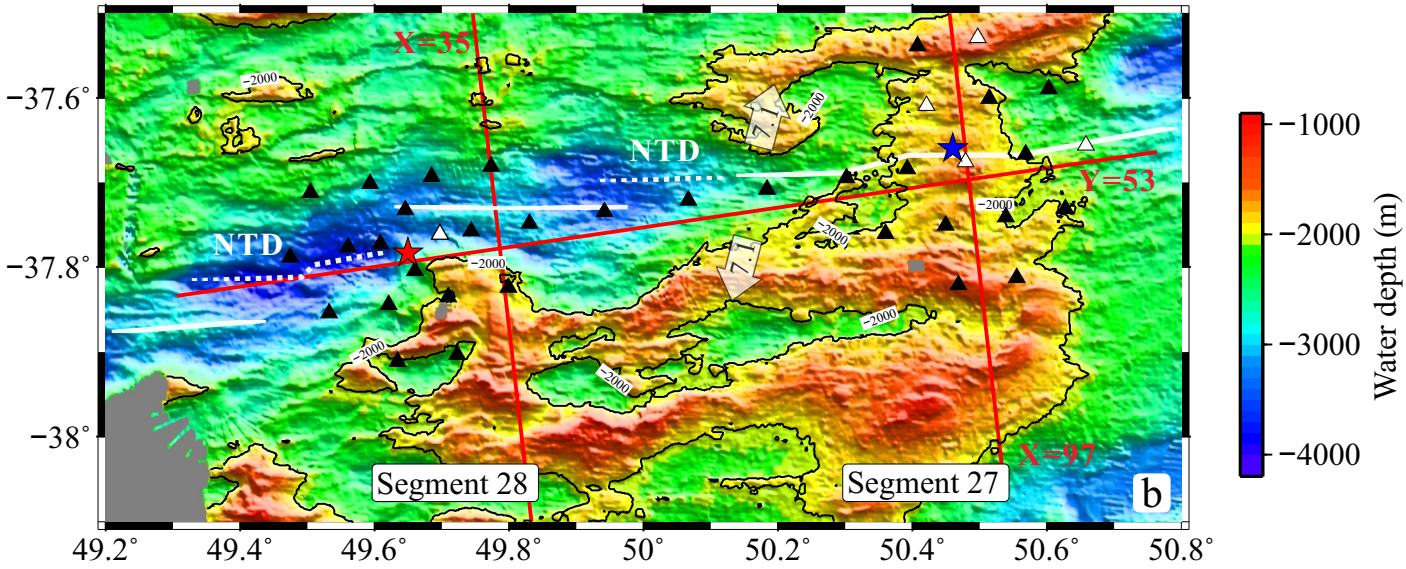
X=35
X=97
Y=53
NTD
NTD
7.1
7.1
−2000
Segment 28
Segment 27
b
−37.6°
−37.8°
−38°
49.2°
49.4°
49.6°
49.8°
50°
50.2°
50.4°
50.6°
50.8°
−1000
−2000
−3000
−4000
Water depth (m)

Figure 2.

2010-02-18 01:42:46s 49.842°E 37.764°S Focal depth: 9.39 km (bsl)

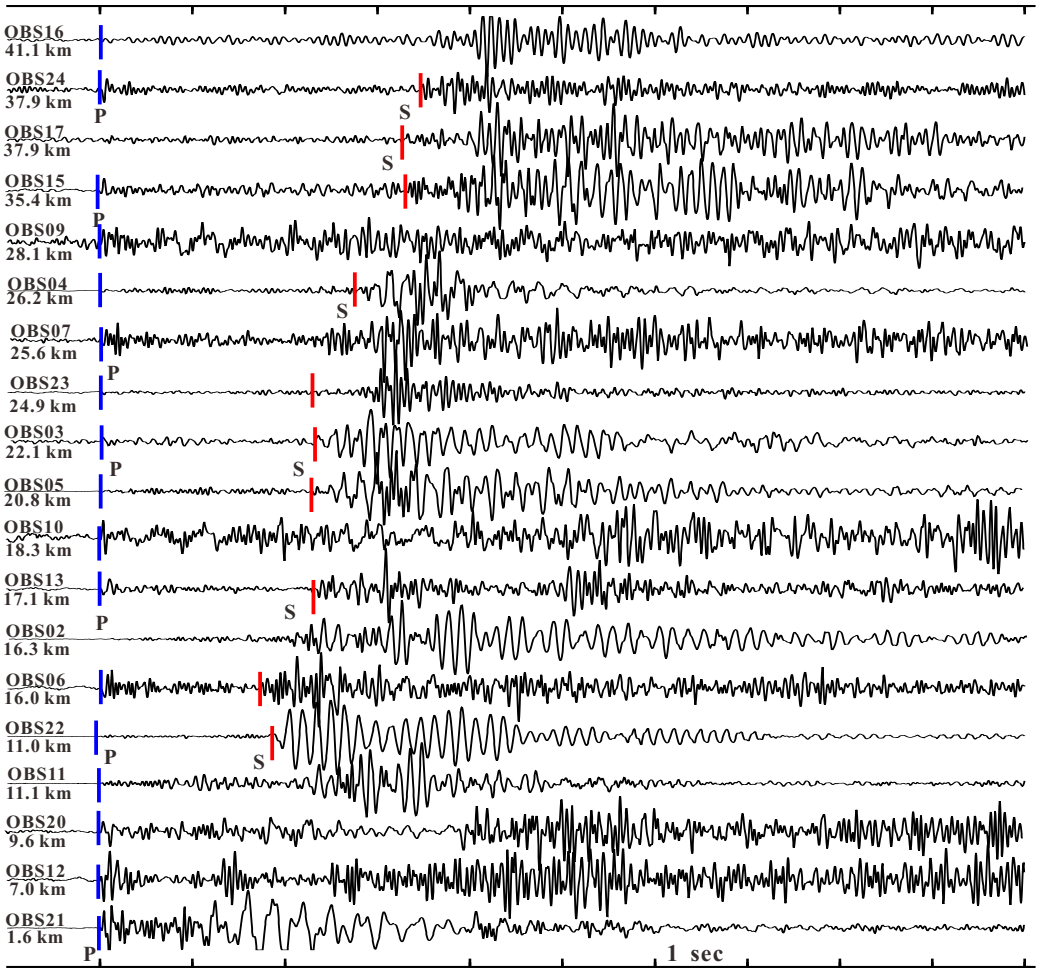

Figure 3.

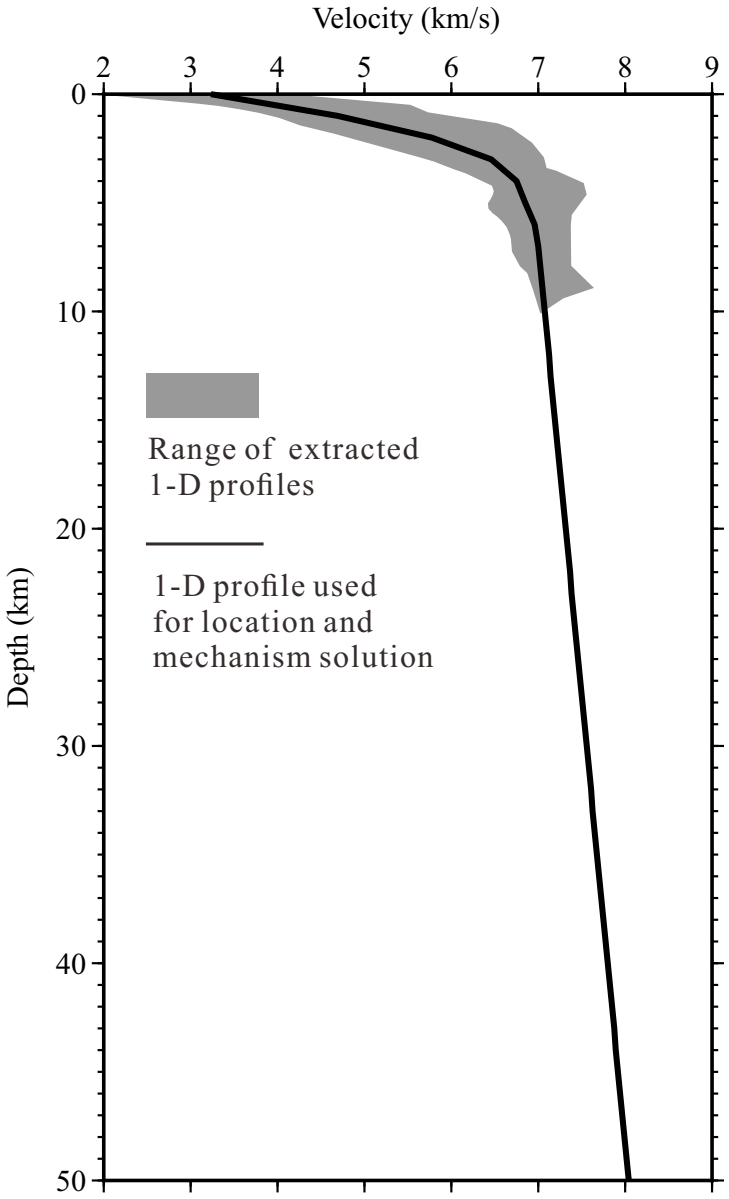
Velocity (km/s)
2
3
4
5
6
7
8
9
0
10
20
30
40
50
Depth (km)
Range of extracted
1-D profiles
1-D profile used
for location and
mechanism solution

Figure 4.

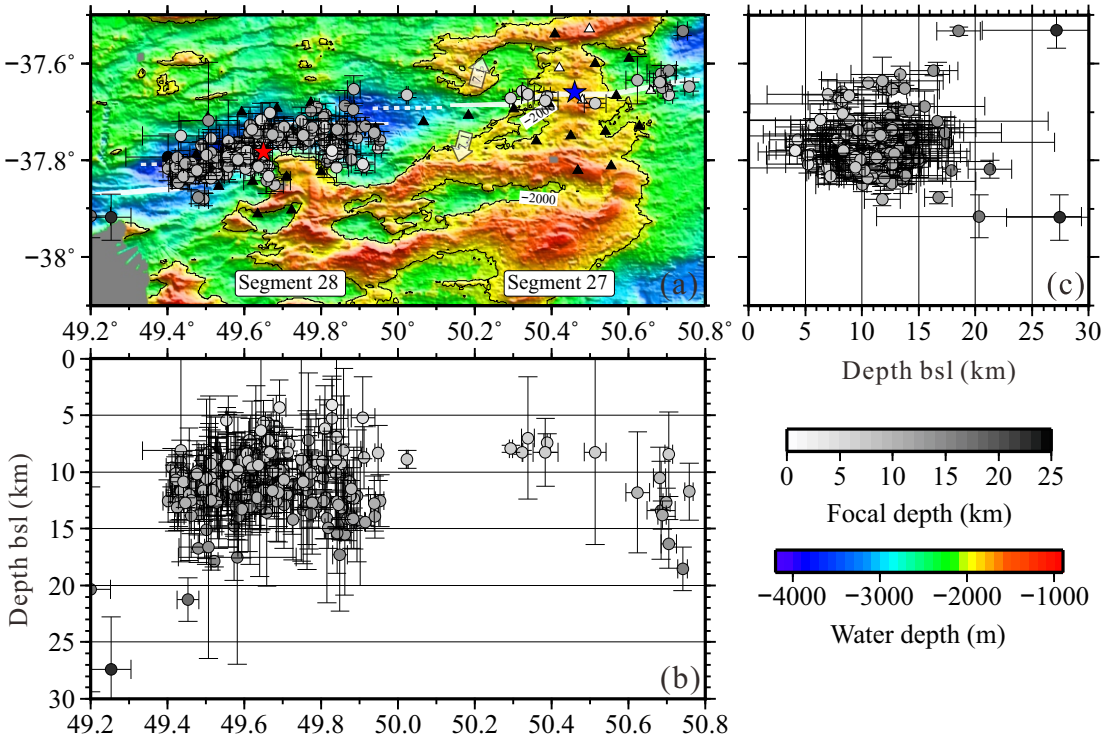
−37.6°
−37.8°
−38°
Segment 28
Segment 27
(a)
−2000
−2000
49.2° 49.4° 49.6° 49.8° 50° 50.2° 50.4° 50.6° 50.8°
(c)
0 5 10 15 20 25 30
Depth bsl (km)
Depth bsl (km)
0 5 10 15 20 25 30
(b)
49.2 49.4 49.6 49.8 50.0 50.2 50.4 50.6 50.8
0 5 10 15 20 25
Focal depth (km)
−4000 −3000 −2000 −1000
Water depth (m)

Figure 5.

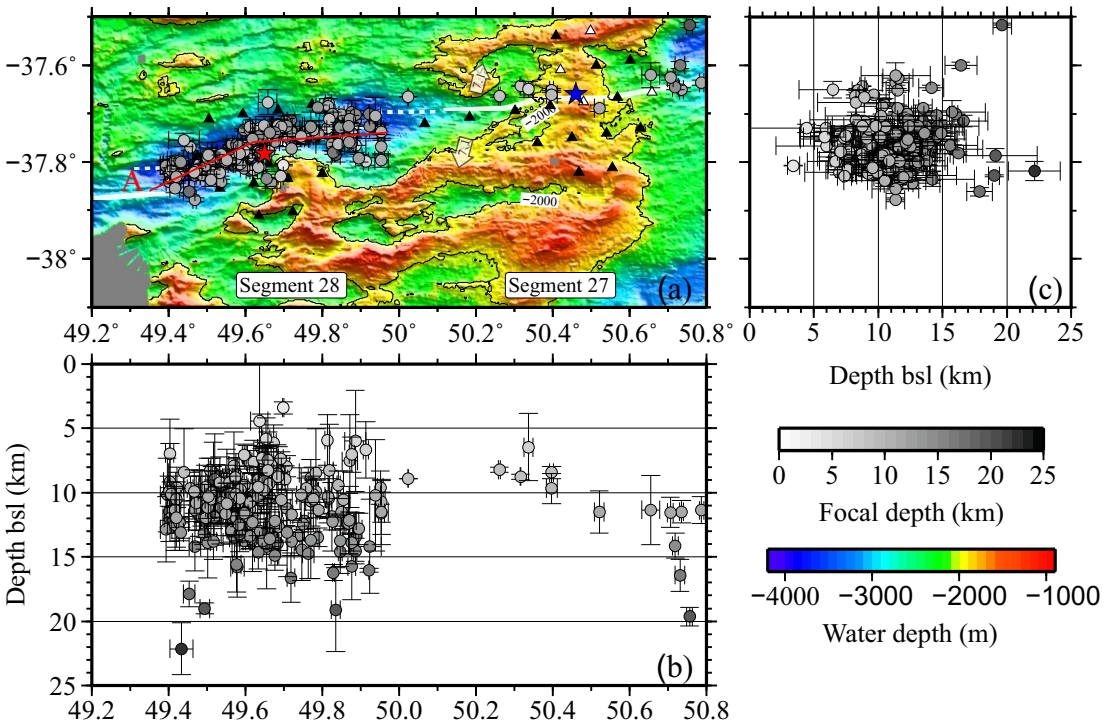
−37.6°
−37.8°
−38°
A
A'
Segment 28
Segment 27
(a)
49.2° 49.4° 49.6° 49.8° 50° 50.2° 50.4° 50.6° 50.8°
(c)
0 5 10 15 20 25
Depth bsl (km)
Depth bsl (km)
0 5 10 15 20 25
49.2 49.4 49.6 49.8 50.0 50.2 50.4 50.6 50.8
(b)
0 5 10 15 20 25
Focal depth (km)
−4000 −3000 −2000 −1000
Water depth (m)

Figure 6.

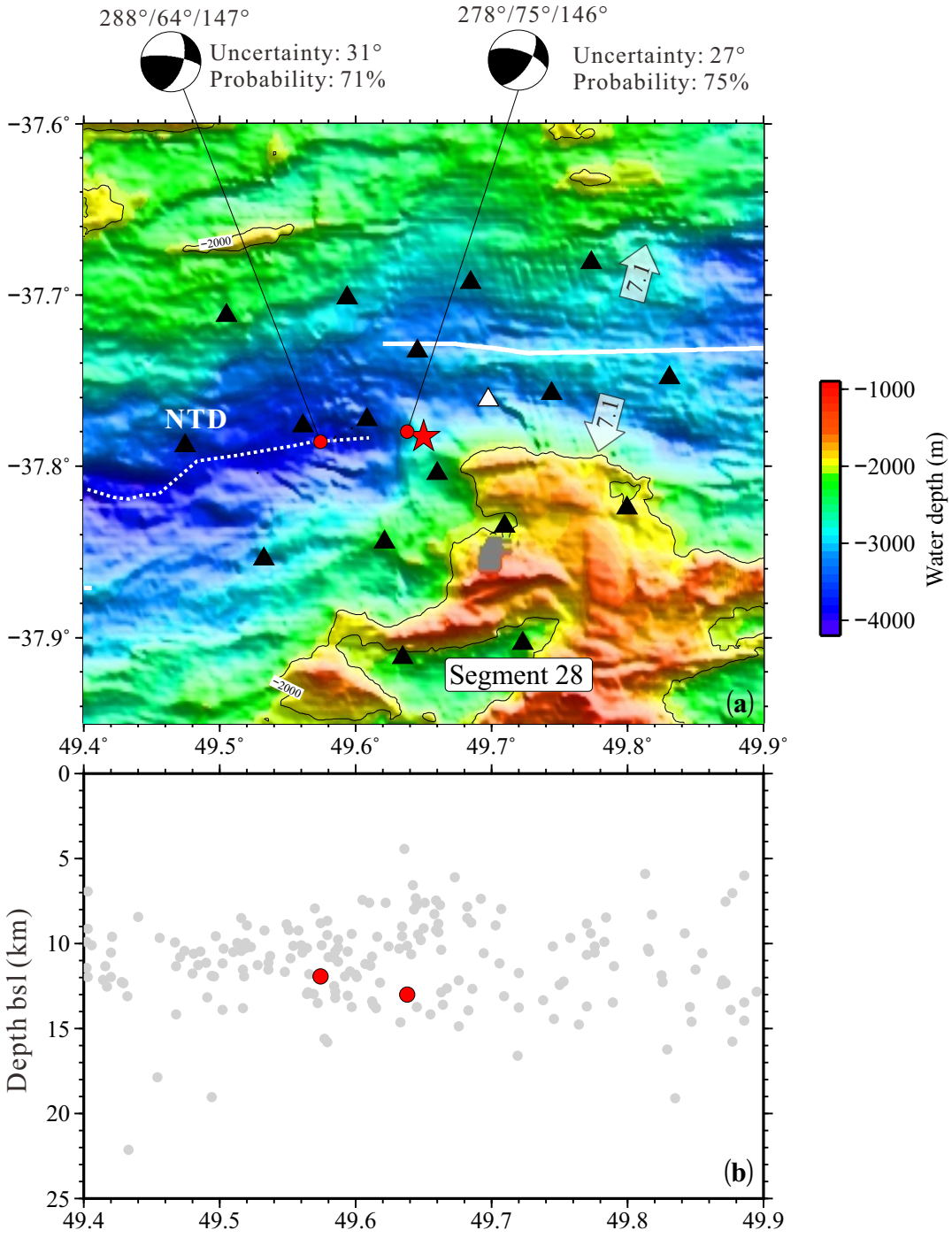
288°/64°/147°
Uncertainty: 31°
Probability: 71%
278°/75°/146°
Uncertainty: 27°
Probability: 75%
−37.6°
−37.7°
−37.8°
−37.9°
−2000
7.1
7.1
NTD
Segment 28
(a)
49.4°
49.5°
49.6°
49.7°
49.8°
49.9°
−1000
−2000
−3000
−4000
Water depth (m)
Depth bsl (km)
0
5
10
15
20
25
(b)
49.4
49.5
49.6
49.7
49.8
49.9

Figure 7.

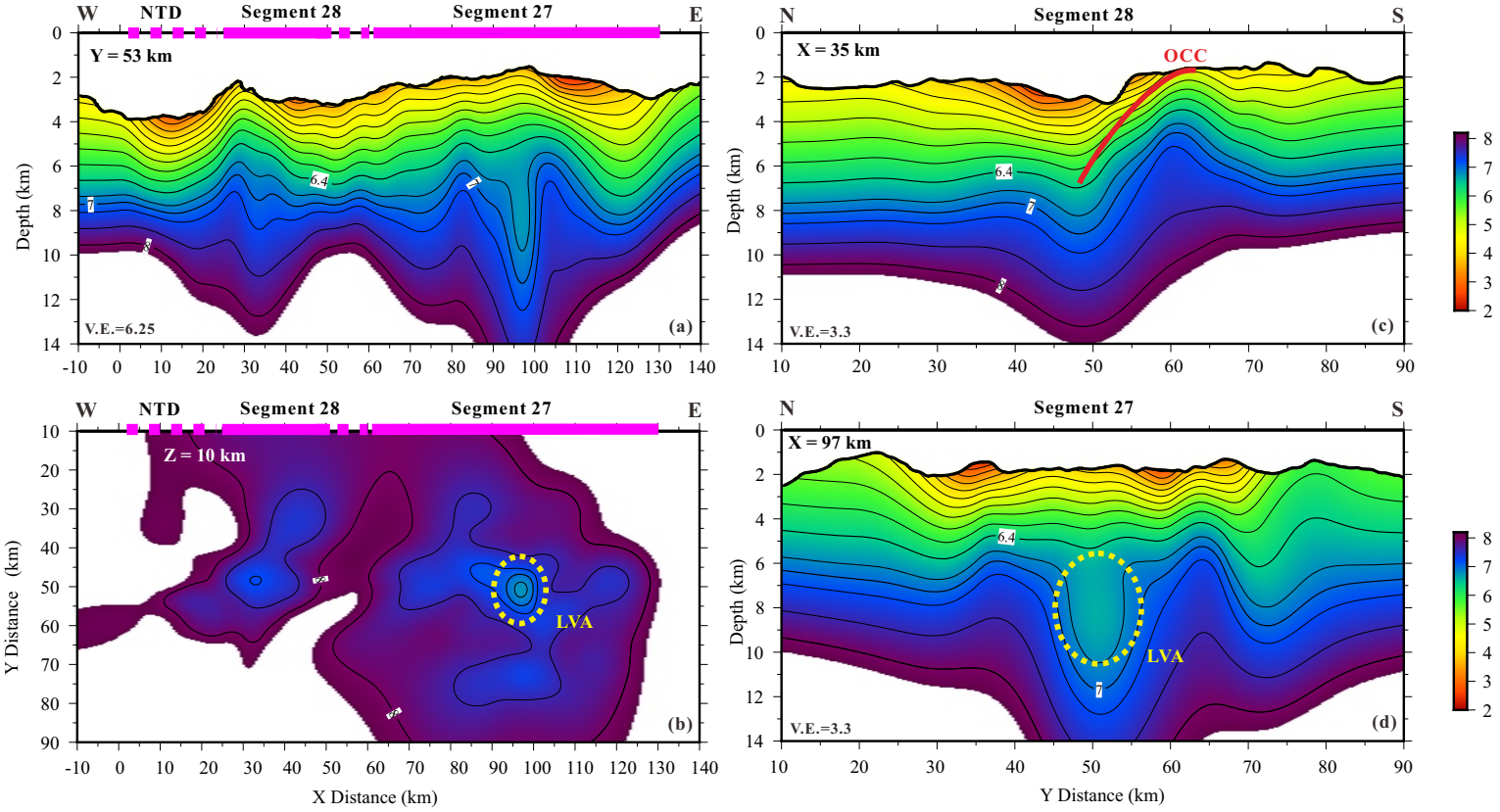
W
NTD
Segment 28
Segment 27
E
Y = 53 km
Depth (km)
6.4
7
8
V.E.=6.25
(a)
N
Segment 28
S
X = 35 km
OCC
6.4
7
8
Depth (km)
V.E.=3.3
(c)
8
7
6
5
4
3
2

W
NTD
Segment 28
Segment 27
E
Z = 10 km
LVA
(b)
Y Distance (km)
X Distance (km)
N
Segment 27
S
X = 97 km
6.4
7
LVA
Depth (km)
V.E.=3.3
(d)
Y Distance (km)
8
7
6
5
4
3
2

Figure 8.

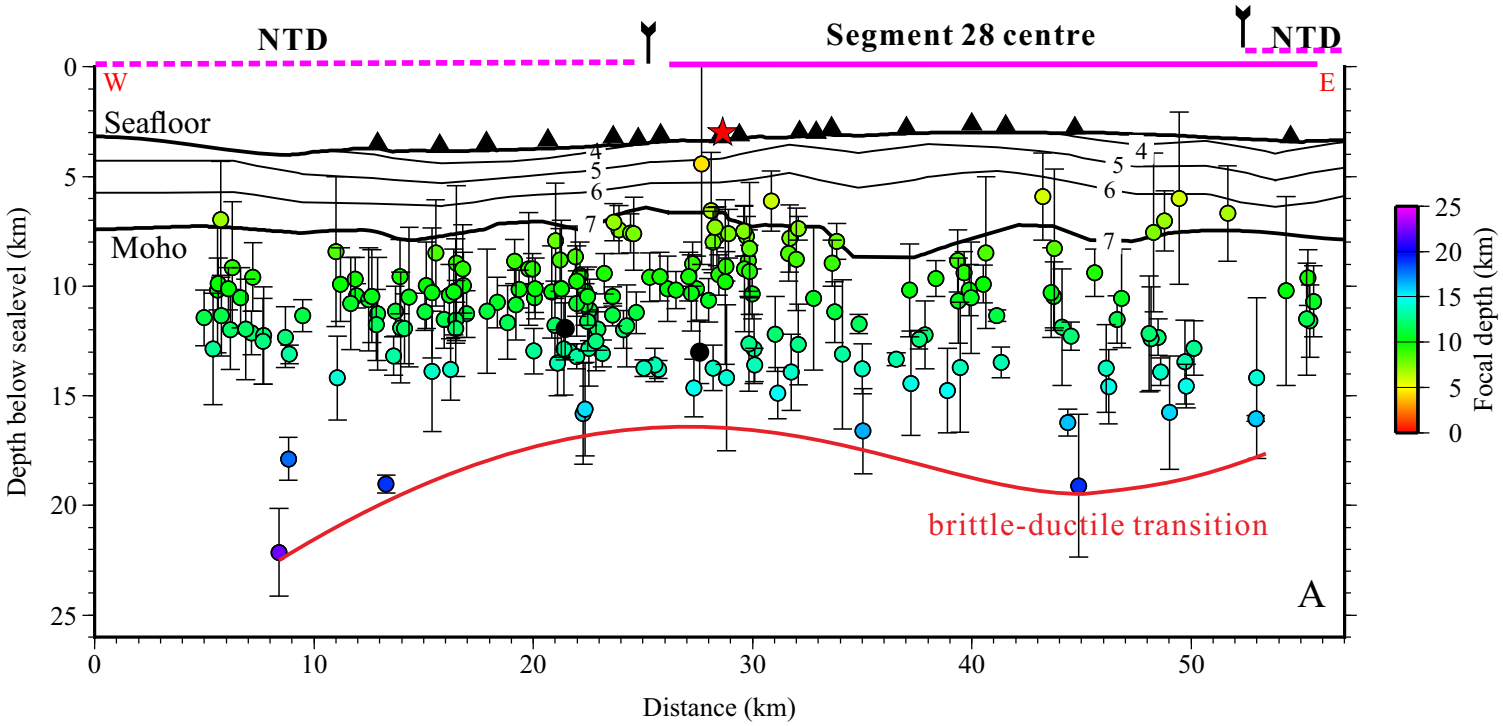
NTD
Segment 28 centre
NTD
W
E
Seafloor
Moho
4
5
6
7
brittle-ductile transition
A
Depth below sealevel (km)
Distance (km)
Focal depth (km)
0
5
10
15
20
25
0
10
20
30
40
50

Figure 9.

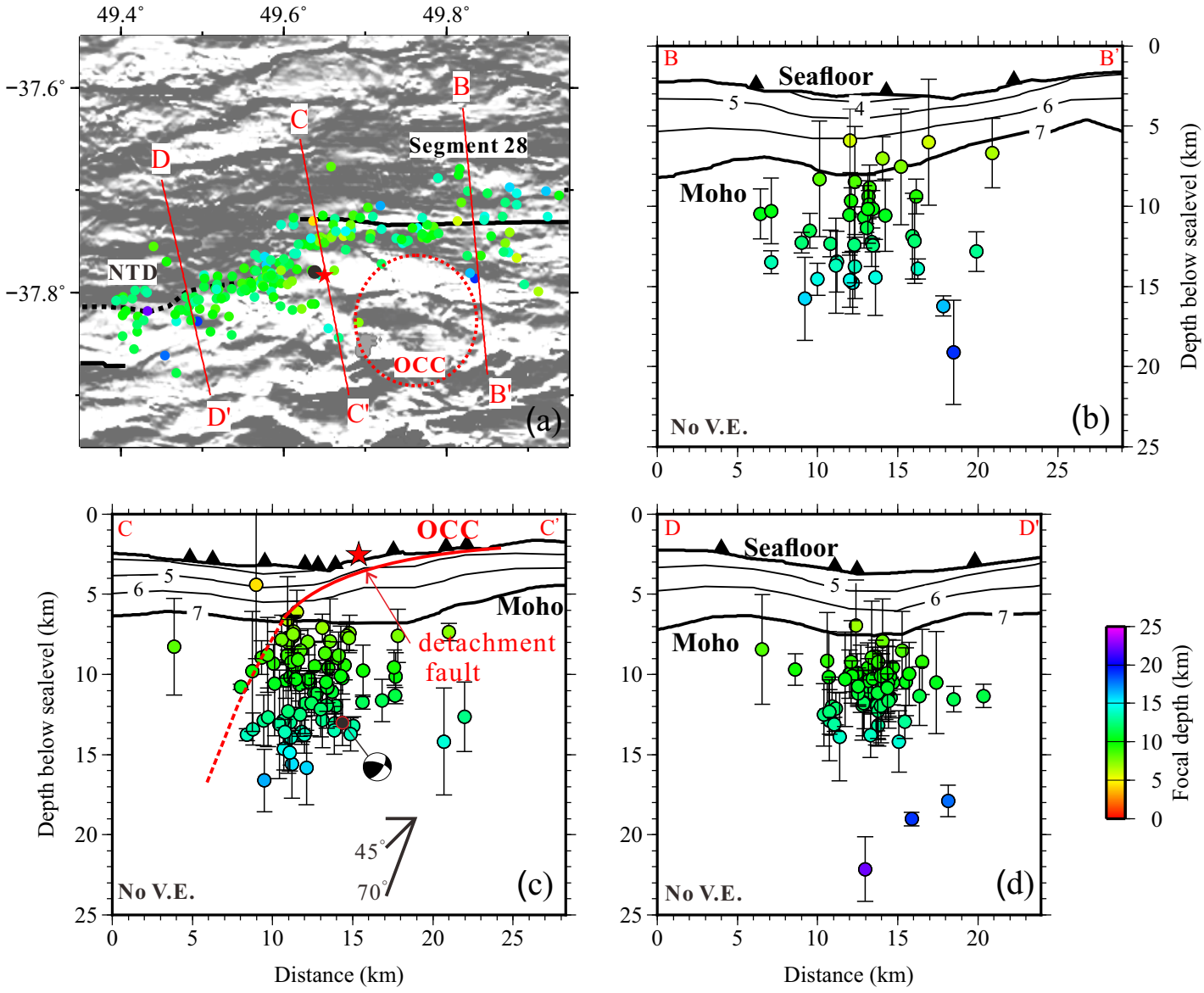
49.4°
49.6°
49.8°
−37.6°
−37.8°
B
C
D
Segment 28
NTD
OCC
B'
C'
D'
(a)
B
B'
Seafloor
Moho
No V.E.
(b)
Depth below sealevel (km)
C
C'
OCC
Moho
detachment
fault
45°
70°
No V.E.
(c)
Depth below sealevel (km)
Distance (km)
D
D'
Seafloor
Moho
No V.E.
(d)
Distance (km)
Focal depth (km)